Hindawi Publishing Corporation
Journal of Nanomaterials
Volume 2016, Article ID 9324858, 10 pages
http://dx.doi.org/10.1155/2016/9324858

Research Article

Effect of TiO_2 Photoanode Porosity on Dye Diffusion Kinetics and Performance of Standard Dye-Sensitized Solar Cells

Cecile Charbonneau, Theo Tanner, Matthew L. Davies, Trystan M. Watson, and David A. Worsley

SPECIFIC, College of Engineering, Swansea University, Baglan Bay Innovation & Knowledge Centre, Central Avenue, Baglan, Port Talbot SA12 7AX, UK

Correspondence should be addressed to Cecile Charbonneau; c.m.e.charbonneau@swansea.ac.uk, Trystan M. Watson; t.m.watson@swansea.ac.uk, and David A. Worsley; d.a.worsley@swansea.ac.uk

Received 13 January 2016; Accepted 3 April 2016

Academic Editor: Meiyong Liao

Low-cost water-based P25-TiO_2 pastes were formulated and used to produce porous TiO_2 films in application to the fabrication of dye-sensitized solar cells. The structural properties of the films were characterized using a variety of techniques such as stylus profilometry, FEG-SEM imaging, BET surface area, and BJH pore size analyses. These were compared to films produced from a commercial paste, DSL 18 NR-AO (Dyesol). The major difference was in the fraction of macroporosity: 23% of the total pore volume for films produced with the commercial material and 67–73% for the P25-TiO_2 films owing to the vast difference in dispersion and size distribution of the particles in the two types of pastes. The macroporosity was found to have a dramatic effect on the dye diffusion kinetics measured using *in situ* UV-Vis reflectance spectroscopy. The sensitization of P25-based films was much faster for heavily macroporous P25-TiO_2 films (>90% saturation at 15–35 mins) than for their commercial analogue (>90% saturation at 110 mins). DSC devices built with optimized P25-TiO_2 photoanodes showed better performance at short dye immersion time (30 mins and 1 hr) due to faster percolation of the dye molecules through the film.

1. Introduction

Research in the field of 3rd generation hybrid organic and inorganic photovoltaic (PV) technologies has seen a drastic change of landscape since the arrival of record photon-to-current efficiency lead-halide perovskite cells, now certified up to 20.1% [1, 2]. The understanding and optimization of this technology has greatly beneficiated from the development of others such as liquid and solid-state dye-sensitized solar cells (DSC) [3]. However, lead-halide perovskite devices still need to overcome a number of problems in terms of materials stability, stabilized current output, and processability. Hence, the scientific community of researchers specialized in the development of 3rd generation PV have continued making parallel progress in optimizing the properties of dye-sensitized solar cells. Recent work dedicated to the development of new dyes and electrolytes led to further improvements in efficiency and stability with devices now reaching 13% efficiency [4] and stabilized outputs for over hundreds of hours [5, 6] for standard laboratory size devices, for example, cells with <1 cm^2 active area. All these efforts contributed to the transfer of DSC technology to the fabrication of larger modules [7, 8] and initial commercial products have been introduced with significant interest in the technology for building integrated photovoltaics [9, 10]. However, the success of DSC devices on the market alongside other competitive photovoltaic technologies (c-Si, CIGS, and CdTe) still depends on the efforts made to address a number of technical, scientific, and process challenges faced in large scale manufacturing.

One major process bottleneck for the large scale production of DSCs is the sensitization of the TiO_2 film, a step achieved in laboratories by immersing a sintered film into a dye solution over night or for periods up to 24 hours. For dye sensitization to be transferable to a roll-to-roll manufacturing process, it is necessary to shorten its duration from hours to seconds, consistent with other process improvements [11, 12].

Several approaches have been suggested to solve this issue, such as pumping the dye solution through the cell [13] and using the benefits of cosensitization to achieve faster dye adsorption [14, 15]. Overall, these developments have led to a significant reduction in the time required to saturate a TiO_2 electrode, which can now be achieved in less than 2 mins [16]. But there is still a need for further improvement of the sensitization process and this can be achieved by controlling structural properties of the TiO_2 film such as the porosity and particle size distribution.

Previous research work has shown that the diffusion of dye molecules through TiO_2 mesoporous films of different thickness, particle size, and porosity is diffusion-limited [17]. This is also true for recently developed electrolytes containing bulkier molecules, such as the Co(II)/Co(III) complexes [18]. Here we have attempted to produce TiO_2 films with a high ratio of macroporosity in order to evaluate its effect on the kinetics of dye diffusion. Not only are the P25-based pastes attractive for their very low production cost, but they have shown promising results in terms of DSC photovoltaic performance [19, 20] when applied in multiple screen printed layers [21–23]. Mixed meso- and macroporous structures resulting from the processing of P25-TiO_2 aqueous pastes have been prepared in our laboratories. Comparison is made with the characteristics of films obtained using a commercial organic-based paste (DSL 18 NR-AO, Dyesol). By applying a method based on UV-Vis reflectance spectroscopy measurements specifically developed in our laboratories for *in situ* monitoring of dye sensitization of TiO_2 thin films [24], we demonstrate here that the use of P25-based pastes with controlled macroporosity can accelerate the dye diffusion process by a factor of 7. It is also suggested that, in addition to the dye diffusion limitation, the kinetics of the dyeing process may be affected by the nature and surface chemistry of the TiO_2 scaffold.

2. Experimental

2.1. Formulation of P25-Based TiO_2 Pastes. The P25-based pastes were prepared by following this simple procedure: 6 g of dry P25- (Degussa) TiO_2 powder was added to an excess (~30 mL) of distilled water at T_{amb} and mixed under magnetic stirring. To promote the dispersion of the particles, 1 mL of concentrated nitric acid (70%) was added to the mixture. Finally, an aqueous solution of polyethylene glycol (PEG 20,000, Fluka) obtained by dissolution of solid flakes of PEG in water at 80°C was added to the TiO_2/HNO_3/water slurries to m(PEG)/m(TiO_2) mass ratios of 0, 10, and 30 wt%. Glass beads were used to add shear to the mixing and the pastes were condensed by evaporation of the excess water under magnetic stirring at 80°C until the TiO_2 content of the paste was 20 wt%. Those three pastes are further referred to as P25-0 wt% PEG (PEG 0), P25-10 wt% PEG (PEG 10), and P25-30 wt% PEG (PEG 30). The commercial DSL 18 NR-AO (Dyesol) was chosen for comparison to the P25-based pastes as it contains mixed TiO_2 nanoparticles and a small fraction of submicron TiO_2 particles, similarly to P25-TiO_2 powders.

2.2. Fabrication of TiO_2 Photoanodes. The titania films were prepared by doctor blading a single layer of an optimized P25-TiO_2 paste or the commercial paste onto precut ($10 \times 2.5\ cm^2$ pieces) transparent conductive glass TEC 15 (15 Ω/cm^2, from NSG Pilkington). Two pieces of Scotch tape 3 M (56 μm) were used as spacers. Sintering of the films was carried out in a preheated oven at 450°C for 30 min. The glass substrates were cut into smaller units ($1.5 \times 2.5\ cm^2$) and photoanodes were shaped into squares of $1 \times 1\ cm^2$ by scratching the contours of the films using a thin microscope coverslip. The thickness and the roughness (R_a) of the films were determined by stylus profilometry, using a Veeco Dektak 150.

2.3. Characterization of the TiO_2 Photoanodes. The top surface of the TiO_2 films was characterized by secondary electron imaging analyses on a S-4800 FEG-SEM apparatus from Hitachi (beam parameters: 1.5 keV, 10 μA). Surface area, pore size distribution, and porosity measurements were performed by nitrogen adsorption using a Tristar II 3020 from Micromeritics. In this case, the films were prepared on microscope coverslips and broken into small pieces for analyses; the contribution of the coverslips in terms of porosity or surface area was measured and found to be negligible.

The BET (Brunauer-Emmett-Teller) surface area is a well-known measurement of the surface area occupied by a monolayer of adsorbed gas molecules (in our case nitrogen) on a porous surface. The BJH (Barrett-Joyner-Halenda) theory is particularly adapted to pore size distribution measurements in the meso- to macroporous range, hence suitable for the films produced in this work.

With the BJH porosimetry measurements, incremental and cumulative volumes of nitrogen filling the pores of the material over a 1.7 to 300 nm range of pore size were collected and used to calculate the porosity (1) and volume fraction of mesopores (2) and macropores (3) of the film:

$$\text{BJH Porosity} = \frac{\text{BJH ads. tot. pore vol. g}^{-1}}{\left(\text{BJH ads. tot. pore vol. g}^{-1} + \left(1/\rho_{TiO_2}\right)\right)}. \quad (1)$$

The density of bulk anatase and rutile was taken as 3.89 g/cm^3 and 4.25 g/cm^3, respectively. Given that P25 contains approximately 80% anatase and 20% rutile, its density is approximately 3.96 g/cm^3, while the DSL 18 NR-AO paste only contains anatase TiO_2 of 3.89 g/cm^3 density:

$$\text{Fraction of mesopores} = \frac{\text{BJH ads. pore vol. of pores} < 50\,\text{nm}}{\text{BJH ads. tot. pore vol.}}, \quad (2)$$

$$\text{Fraction of macropores} = \frac{\text{BJH ads. pore vol. of pores} > 50\,\text{nm}}{\text{BJH ads. tot. pore vol.}}. \quad (3)$$

2.4. Diffuse Reflectance UV-Vis Spectroscopic Measurements. The method used to collect the dye uptake kinetics is fully

described in a separate paper [24]. Briefly, in this study, the films were prepared on nonconductive silica glass and shaped into squares of $2 \times 2\,\text{cm}^2$ area. The films were rinsed with ethanol and a plastic open screw top was sealed around the films by application of a silicon rubber (RS 494-118). The diffuse reflectance UV-Vis spectroscopy measurements were performed with a Perkin Elmer Lambda 750S (60 mm integrating sphere). The samples were vertically positioned against the reflectance opening of the integrating sphere so that the centre of the TiO_2 film was aligned with the beam path. The spectra were recorded between 250–800 nm at 5 min intervals. A spectrum of the bare TiO_2 film was acquired to further correct for its contribution on the spectra acquired during real time monitoring the dye diffusion. The dye solution was poured inside the plastic screw top container and the sample was immediately placed inside the UV-Vis spectrometer and the data acquisition was launched (this process took no longer than 10–15 s). The uptake of N719 was monitored by plotting the intensity of the absorbance spectra at $\lambda = 540$ nm (the wavelength of maximum absorbance of the N719 dye) against time. On the absorbance graphs produced in this paper, the data were normalized according to the maximum absorbance value recorded (assumed to correspond to the dye saturation of the pores) and $t = 0$ corresponds to the time when the data collection was started.

2.5. Comparative Dye Desorption UV-Vis Measurements. To correlate the results obtained in real time diffuse reflectance UV-Vis spectroscopy measurements, dye desorption experiments were carried out. Strips of TiO_2 films were prepared according to the fabrication method previously described, this time using $10 \times 2.5\,\text{cm}^2$ nonconductive glass substrates carefully weighed before and after the deposition of the TiO_2 film. These films were immersed in a dye bath during 30 mins, 1 hr, and 24 hrs at T_{amb}, rinsed with ethanol, and dried. The films were then separately immersed in 100 mL of a solution of 0.1 M sodium hydroxide (NaOH), forcing the dye molecules to desorb from the surface of the TiO_2 films. Samples of the solution were analyzed by UV-Vis spectroscopy absorbance measurements in quartz cuvettes against a blank solution of 0.1 M NaOH. The concentration of dye molecules after desorption depends on the total surface area of TiO_2 available for each film. This parameter is often disregarded in literature but is of great importance here since the TiO_2 scaffolds considered in this study have variable surface areas and are likely to accommodate a variable number of dye molecules. Hence, the absorbance data reported for solutions containing the desorbed dye molecules were corrected as follows:

$$\text{Corrected Absorbance} = \frac{\text{Absorbance}}{\text{Weight}\left(TiO_2 \text{ film}\right) \times SA_{\text{BET}}}. \quad (4)$$

The intensity of the corrected absorbance data at $\lambda = 540$ nm, which is proportional to the concentration of desorbed dye molecules according to the Beer-Lambert law, was used to monitor the evolution of the amount of dye adsorbed at 30 mins, 1 hr, and 24 hrs.

2.6. Dye Sensitization, Device Assembly, and Testing. The fabrication of the photoanodes used in DSC devices involved the preparation of a single layer of porous TiO_2, without any scattering layer. This allowed correlating the pore size distribution of the active layer to the kinetics of dye uptake and cell performance. In reality, if such materials were scaled to commercial use, it is likely that a double layer of paste would be applied together with a scattering layer to maximise surface area and hence photon capture and efficiency.

The films were sensitized for various amounts of time: 30 mins, 1 hr, and 24 hrs by immersion in a 3 mM dye solution bath at T_{amb}. The dye solution was prepared by dissolving *cis*-bis(isothiocyanato)bis(2,20-bipyridyl-4,40-dicarboxylato)-ruthenium(II)bis-tetrabutyl-ammonium (N719, Dyesol) in ethanol, assisted with ultrasonic agitation at T_{amb} for 1 hr. The films were further rinsed with ethanol and dried in air.

Counter electrodes were prepared on precut $1.5 \times 2.5\,\text{cm}^2$ pieces of TEC 15 ($15\,\Omega/\text{cm}^2$ FTO coated glass from NSG). A hole was drilled in preparation for electrolyte insertion, using a 0.5 mm drill bit. A 5 mM solution of chloroplatinic acid (H_2PtCl_6, Sigma Aldrich) in isopropanol was spread on the conductive side of the glass substrates and held in a preheated oven at 385°C for 30 min to platinise the FTO.

Laser cut 25 μm thick Surlyn gaskets (Solaronix) were cleaned with isopropanol and dried before application. Sealing of the working and counter electrodes was performed using a hot press at 120°C for 1 min. A standard I^-/I_3^- based electrolyte (0.8 M 1-propyl-3-methylimidazolium iodide (PMII), 0.3 M benzimidazole, 0.1 M I_2, and 0.05 M guanidinium thiocyanate dissolved in 3-methoxypropionitrile, all components from Sigma Aldrich) was vacuum filled through the predrilled hole. The hole was sealed by melting a small piece of Surlyn underneath a circular microscope coverslip. Silver conductive paint was applied along the edges of the electrodes for optimization of current collection.

The photovoltaic performance of assembled DSCs was tested using the Oriel Sol 3A solar simulator (equipped with a Xenon arc lamp) under normal illumination at 1 sun ($1000\,\text{W/m}^2$, 1.5 AM). The lamp output was calibrated with a reference silicon solar cell.

3. Results and Discussion

3.1. Structural Properties of the TiO_2 Photoanodes. Titania films were produced by application of the different pastes described in Experimental; in all cases, a minimum of 3 samples of each paste were prepared to monitor the reproducibility of the data. The thickness and R_a roughness of the films were measured and averaged over a distance of 1 cm, as reported in Table 1. The profilometry scans showed the average thickness of the films to decrease with an increasing content of PEG used in the paste: 14.2 (±2.9) μm, 12.0 (±1.5) μm, and 9.3 (±0.8) μm for PEG 0, PEG 10, and PEG 30 films. This is thought to relate mostly to improved particle dispersion: upon addition of the binder, the viscosity of the paste visibly increased and the shear forces exerted on the particles

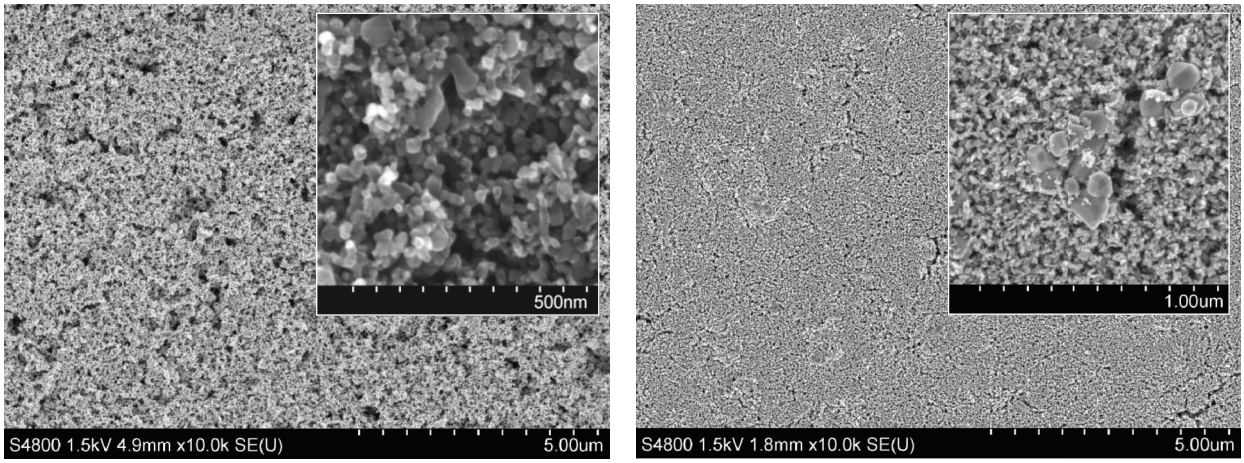

(a) (b)

Figure 1: Top view FEG-SEM images of films prepared with pastes PEG 30 (a) and DSL 18 NR-AO (b).

Table 1: Average thickness and roughness (R_a) of TiO_2 films.

Sample	Thickness (μm)	R_a (nm)
PEG 0	14.2 (±2.9)	580 (±310)
PEG 10	12.0 (±1.5)	410 (±70)
PEG 30	9.3 (±0.8)	210 (±50)
DSL 18 NR-AO	9.7 (±0.1)	210 (±20)

forced large aggregates to collapse into smaller units. The introduction of increasing amounts of PEG improved the reproducibility of the film thickness characteristics, with variations decreasing from 20 to 12.5 and 9% of the average height. Additionally, increased amounts of binder were found to improve the stability and homogeneity of particle dispersion over long storage times. In comparison, films prepared with the DSL 18 NR-AO, a paste characterized with much higher viscosity owing to its terpineol content, were characterized with a reproducible average thickness of 9.7 ± 0.1 μm. Roughness measurements (R_a) showed that the addition of PEG to P25-based pastes led to an important decrease in surface roughness, with average R_a values of 580 (±310) nm (PEG 0), 410 (±70) nm (PEG 10), and 210 (±50) nm (PEG 30). The latter compares to an average R_a of 210 (±20) nm obtained for films prepared with the DSL 18 NR-AO paste.

Top view electron microscope images of films prepared with PEG 30, one of the P25-based pastes, and DSL 18 NR-AO are presented in Figure 1. A similar investigation was performed on films prepared with the PEG 0 and PEG 10 pastes which showed very similar characteristics to the film prepared with PEG 30. When comparing the structure of films obtained from PEG 30 and DSL 18 NR-AO pastes, the first noticeable difference lies in the density of the particle networks. The structure of the P25-based film appears to hold a wide range of pore sizes while the DSL 18 NR-AO is characterized with a uniformly porous and much denser network of particles. In particular, the appearance of macropores (pore size > 50 nm) can be observed at the surface of the PEG 30 film and hypothetically in its inner structure. In the case of the DSL 18 NR-AO film, the only macropores visible are caused by the presence of few larger scattering particles of *ca.* 100 nm in diameter (Figure 1(b) insert).

The second main observation is related to the difference in particle size: P25 powder contains approximately 80% anatase and 20% rutile with an average primary particle size of 21 nm and a broad particle size distribution (Figure 1(a) insert) while the DSL 18 NR-AO paste mostly contains 20 nm average size anatase particles with a very narrow particle size distribution completed by a small fraction of submicron scattering particles (Figure 1(b) insert).

Porosity measurements were performed on films prepared on nonporous thin coverslip glass slides with negligible surface area (sintered at 450°C for 30 min). Table 1 presents, for each film, the values of porosity (total volume fraction of pores in the film), cumulative pore volume and area, and volume fraction of pores in the mesoporous and macroporous range. These values were extracted from BJH adsorption and BET surface area data collected in the pore size range 1.7–300 nm. Figure 2 presents diagrams showing the BJH pore size distribution, adsorption, and desorption isotherms (inserts) for each film. P25-based films were found to have cumulative pore volumes in the range 0.372–0.429 cm^3/g, corresponding to 59.8–63.2% overall porosity, for example, the volume occupied by pores as opposed to solid TiO_2 particles in the film. This is higher than the porosity of the DSL 18 NR-AO film characterized with a cumulative pore volume of 0.336 cm^3/g equivalent to 56.6% porosity, reflecting the denser particle network of the material. These results correlate precisely the microscopic observations presented in Figure 1. All isotherms presented in Figure 2 are characterized with a shape of type IV with a narrow hysteresis located in the P/P_0 range 0.9–1, indicative of porous materials with a mixed mesoporous (2–50 nm pore size) and macroporous (>50 nm pore size) structure. This is confirmed by the pore size distribution diagrams: the films derived from P25-based pastes are seen to be characterized with broad pore size

Table 2: Porosity and surface area characteristics of films prepared with pastes PEG 30 and DSL 18 NR-AO.

Sample	BJH adsorption cumulative pore volume (cm^3/g)	BJH porosity (%)	BJH volume % of mesopores	BJH volume % of macropores	BET surface area (m^2/g)
PEG 0	0.372	59.8	32	67	42.4 (±0.1)
PEG 10	0.404	61.8	29	71	45.7 (±0.1)
PEG 30	0.429	63.2	27	73	44.8 (±0.1)
AO	0.336	56.6	77	23	52.9 (±0.2)

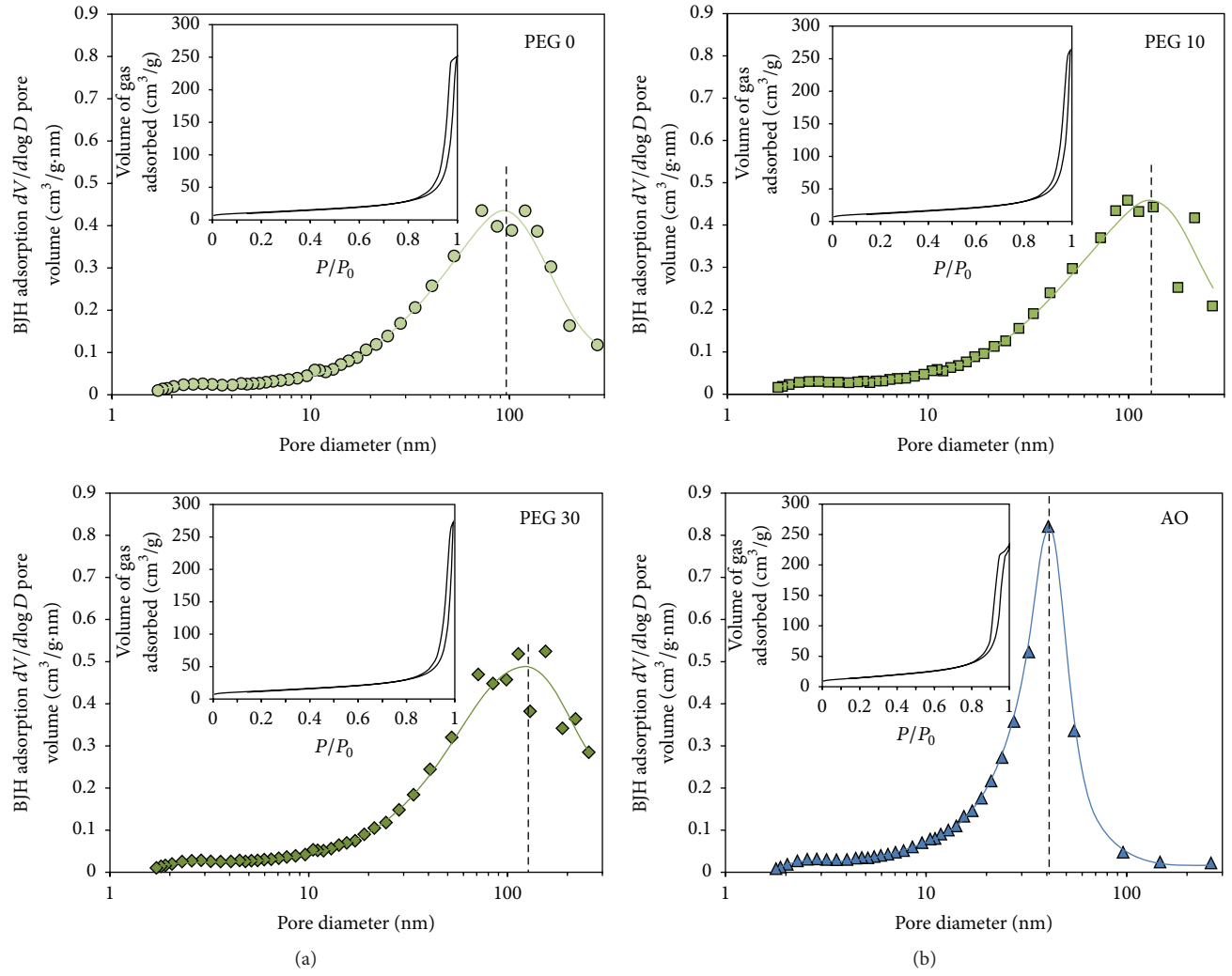

Figure 2: Pore size distribution and isotherms (inserts) of films prepared with PEG 30 (a) and DSL 18 NR-AO (b).

distributions ranging from approximately 2 to 300 nm (the upper BJH pore diameter limit of the apparatus) and 2 to 100 nm in the case of the DSL 18 NR-AO film. The cumulative contribution of each type of pores, mesopores versus macropores, was evaluated based on the BJH pore volume data collected for each film (Table 2). These data demonstrate the structure of P25-based films to be characterized with a large amount of macropores, namely, 67–73% of the total pore volume, while the porous structure of the DSL 18 NR-AO film consists mostly of mesopores, namely, 77% of its total pore volume. Such difference can be explained by considering several factors: (1) P25-TiO_2 powder tends to be produced in the form of aggregates owing to the nature of the fabrication process while the anatase TiO_2 particles used for the fabrication of the DSL 18 NR-AO are produced by a highly dispersive sol-gel process and (2) the content and the nature of the binders used in the different pastes are important parameters controlling the pore size distribution of resulting films, (3) but most essentially here the degree of mixing and associated dispersion of the particles in the paste has a critical

impact on the pore size distribution of the films. This is very clear from the broad pore size distributions observed for P25-based films in Figure 2, indicative of the presence of aggregates which could not be separated during the paste preparation process. However, increasing amounts of binder were found to further broaden the pore size distribution and shift the population maxima (dash lines) from 95 nm to 120 nm and from 130 nm for films prepared with PEG 0, PEG 10, and PEG 30, respectively. These observations are thought to relate to the presence of aggregated or poorly dissolved flakes of binder material responsible for the creation of a new population of macropores. This trend is in agreement with the increased volume fraction of macropores from 67 to 71 and 73% calculated for films produced using PEG 0, PEG 10, and PEG 30 pastes, respectively. In contrast, film DSL 18 NR-AO displays a much narrower pore size distribution with a maximum at 41 nm, typical of a film produced from a paste with very homogeneous particle dispersion. Finally, the data presented in Table 2 show that the DSL 18 NR-AO film has a surface area of 52.9 m^2/g, which is larger than the surface area of the P25-based films, ranging from 42.4 to 45.7 m^2/g. This result is in agreement with the denser particle network and slightly smaller average primary particle size of the DSL 18 NR-AO film compared to the P25-based film.

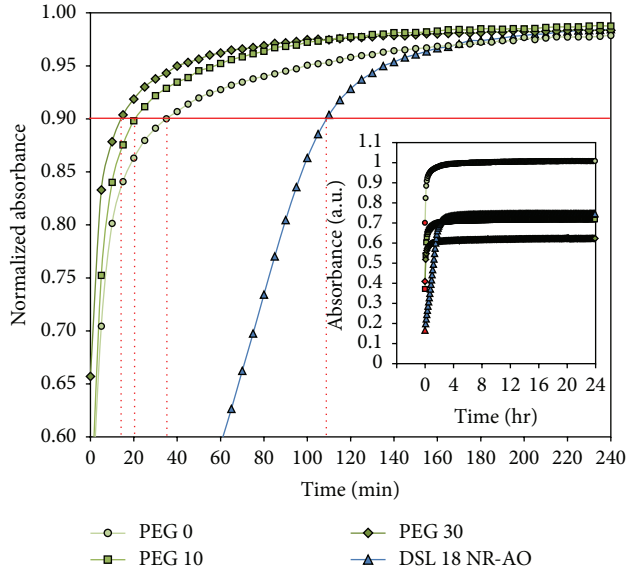

Figure 3: Normalized and raw data (insert) absorbance at λ = 540 nm of real time diffuse reflectance UV-Vis spectroscopic measurements of TiO_2 films immersed in a 3 mM ethanolic N719 dye solution. The red symbols correspond to the first absorbance value collected after introduction of the dye solution.

3.2. Effect of the Photoanode Structure on the Kinetics of Dye Diffusion. It is known from other studies [17, 24] that the concentration of the dye solution and film thickness are important parameters to consider when studying the kinetics of dye uptake in TiO_2 photoanodes because of its predominant diffusion-controlled nature. Here, the concentration of the dye solution was fixed at 3 mM and the films prepared for this part of the study were first characterized in terms of thickness, respectively, 13.8 (±4.1) μm, 11.6 (±1.8) μm, 9.3 (±0.5) μm, and 8.9 (±0.4) μm for films PEG 0, PEG 10, PEG 30, and DSL 18 NR-AO.

In order to evaluate the effects of the porosity changes on the kinetics of dye diffusion, a study of the degree of colour uptake by the different film types was undertaken using real time DR UV-Vis, a technique described in previous work [24]. Figure 3 shows the evolution of the maximum normalized absorbance of each sample (at 540 nm), representative of the amount of dye percolated through the TiO_2 film, as a function of time. All plots show a fast initial increase of the absorbance up to around 90% of the saturation point, followed by an abrupt deceleration of the trend until the absorbance values reach a plateau corresponding to the dye saturation of the film. A normalized absorbance value of 0.9 is assumed to reflect an average level of dye concentration of at least 90% of its saturation level throughout the entire thickness of the film. A fraction of the dye molecules is chemically adsorbed to the surface of the TiO_2 particles while others are still in suspension inside the pores of the film. In this work, no solution agitation was employed and the work was done at normal room temperature (ca 25°C). A two-phased kinetic process was already reported and characterized in a previous study [24]. The two phases are thought to be related, first, to the fast diffusion of the dye molecules through the film along with simultaneous adsorption by chemical bonding at the surface of the bare TiO_2 particles and, second, to the filling of the remaining vacant adsorption sites. Hence, the kinetics of the first phase of dye uptake is mainly diffusion-controlled, while in the second phase, it is rather dominated by slower mass transfer principles. Despite the variations reported in terms of film thickness, the plots presented in Figure 3 show the first phase of dye uptake to be much faster in the case of the P25-based films, with 90% dye saturation reached after 15, 20, and 35 min, respectively, for films PEG 0, PEG 10, and PEG 30, compared to 110 mins for the DSL 18 NR-AO film. It appears from those results that the porous characteristics of the films have a considerable impact on the kinetics of dye diffusion for films of comparative thickness.

The data presented in the insert of Figure 3 correspond to the raw absorbance data corrected for the absorbance of the TiO_2 film before introducing the dye solution. The maximum absorbance (Abs_{max}) data collected at 24 hrs correlate structural differences between the films in terms of thickness and surface area: (1) for the P25-based films, PEG 0, 10, and 30 of decreasing thickness, Abs_{max} at 24 hrs is observed to decrease proportionally to the thickness and (2) when comparing films PEG 30 and AO, of similar thickness, a higher Abs_{max} is collected at 24 hrs for film AO compared to film PEG 30, which is directly related to the difference in surface area (52.9 versus 44.8 m^2/g).

In order to discriminate between the influence of the overall porosity and the pore size distribution of the films on the kinetics of dye diffusion in the first phase, the time to a normalized absorbance value of 0.9 (i.e., 90% dye uptake) was plotted as a function of the values reported in Table 1 under "porosity" and "fraction of macropores." The corresponding diagram is presented in Figure 4. It shows

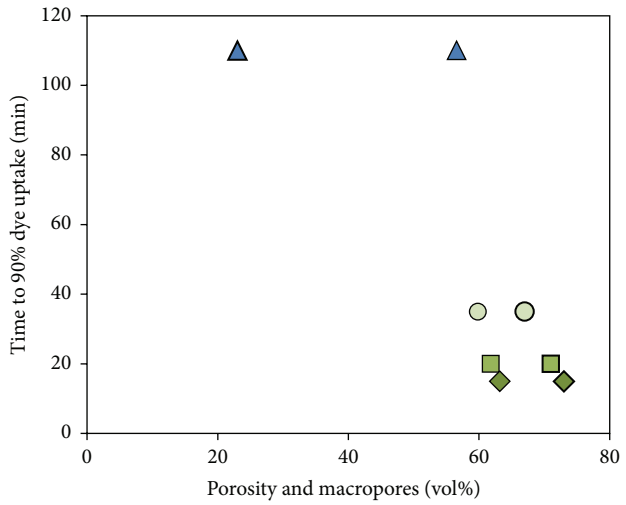

FIGURE 4: Influence of the porosity (thin contour) and percentage of macropores (thick contour) on the kinetics of dye uptake for the AO (triangle), PEG 0 (circle), PEG 10 (square), and PEG 30 (diamond).

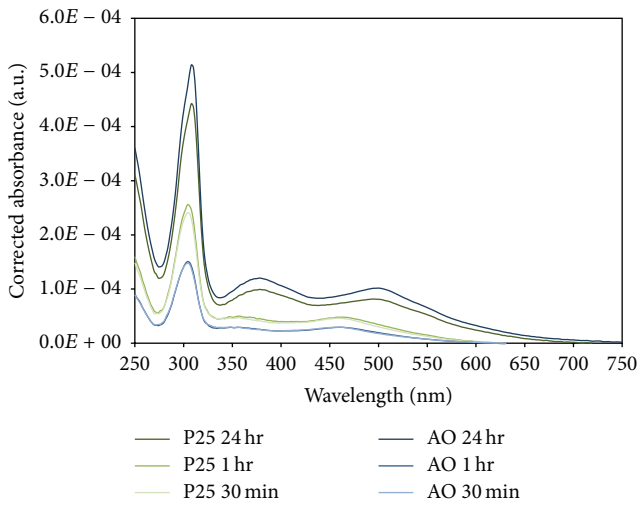

FIGURE 5: Dye desorption of sintered TiO_2 films immersed for 30 mins to 24 hrs in a 3 mM solution of N719 dye in ethanol. The absorbance was corrected for the actual specific surface area of each film, where Corr. Abs = Abs./(SA_{BET} × weight).

that the kinetics of dye diffusion in the first phase fastens in parallel with an increase in overall porosity and an increasing fraction of macropores. The overall porosity seems to be the dominant factor, an indication that the dye diffusion process may be critically accelerated by controlling the density of the photoanode. The beneficial effects of a wide pore size distribution and more specifically the presence of macropores on the percolation of species through porous materials have already been reported in other studies [25, 26]. However, to the best of our knowledge, it is the first time that parameters such as the porosity and the intentional introduction of a large fraction of macropores within the TiO_2 photoanodes are reported to accelerate the process of dye diffusion specifically for the fabrication of DSC photoanodes. This finding is significant since it offers an additional method for accelerating the slow process of dye uptake. This may also be combined with existing techniques such as fast flow of the dye and high temperature dyeing. Moreover, this finding may be of paramount importance for the improvement of DSC technologies based on the use of liquid electrolytes with large cations such as the Co(II)/Co(III) system, where slow mass transport of the redox species through the mesoporous network of TiO_2 particles (where the diffusion coefficient is typically one order of magnitude lower than in I^-/I_3^- systems) currently limits the output performance of devices [18]. The next part of this work further demonstrates the positive impact of porosity on accelerated dyeing based on DSC device performance at various dyeing times.

3.3. Dye Desorption Study and Performance of DSC Photovoltaic Devices. A series of six TiO_2 strips was produced on FTO glass using the PEG 30 paste, for which the fastest dye diffusion kinetics was observed, and DSL 18 NR-AO. These were immersed in an ethanolic N719 dye solution for 30 mins, 1 hr, or 24 hrs. The weight of each TiO_2 strip was measured carefully in order to calculate the specific surface area of TiO_2 particle network available for the adsorption of the dye molecules. The anchored dye molecules were forced to desorb by dipping the FTO/N719-TiO_2 strips in a basic solution; absorbance data were collected in transmission for each of the solutions and divided by the surface area of each film as explained in further detail in Experimental and reported in Figure 5. The data show that, for each type of TiO_2 photoanode, the number of dye molecules adsorbed increased with time. Although the amount of dye adsorbed at 30 mins and 1 hr is very similar for the two types of TiO_2 films, there is a significant increase between 1 hr and 24 hrs dye immersion. This phenomenon was discussed in previous work [11] and may be attributed to (1) an initial phase during which a fast saturation of the TiO_2 pristine surface with diffused dye molecules is seen, followed by (2) a slow second phase during which the dye molecules reorganize themselves at the surface of the TiO_2 particles, allowing a higher density of dye molecules to anchor. When comparing the results obtained with PEG 30 and DSL 18 NR-AO photoanodes at equal immersion times, the corrected absorbance obtained for PEG 30 at 30 mins and 1 hr is significantly higher than in the case of DSL 18 NR-AO. This is indicative that the diffusion of dyes through the largely macroporous P25-based films is much faster than through the highly mesoporous DSL 18 NR-AO films, an advantage in terms of manufacturing. At 24 hrs, the absorbance of the dye solution recovered from the DSL 18 NR-AO film becomes higher than for P25-based film. This may relate to the surface chemical properties of the two TiO_2 nanomaterials. TiO_2 P25 nanoparticles tend to exhibit very high hydrophilic properties compared to sol-gel processed TiO_2 materials typically used in the formulation of commercial paste products. Hence, the use of P25-TiO_2 particles may favour the adsorption of "parasitic" water molecules from the environment which can locally inhibit the anchoring of dye molecules.

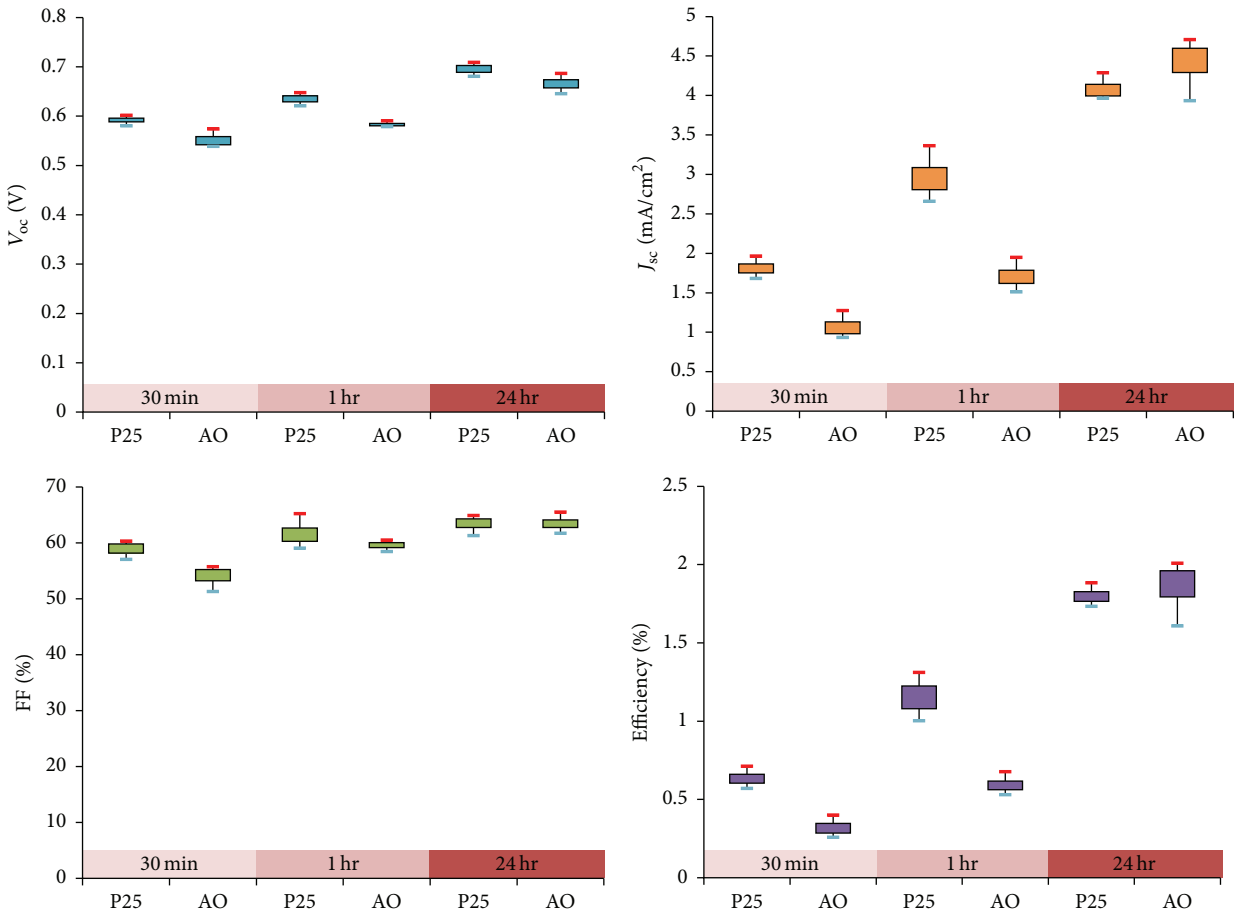

FIGURE 6: Light-to-current conversion efficiency of dye-sensitized solar cells prepared with the PEG 30 and DSL 18 NR-AO pastes, immersed in a 3 mM N719 dye solution for 30 mins, 1 hr, and 24 hrs, and tested under 1 sun (1000 W/m^2, 1.5 AM) illumination.

The same procedure was repeated to fabricate photoanodes used to build dye-sensitized solar cells with an active area of 1 cm^2. Five identical cells were built for each type of photoanodes; the architecture of these cells was not optimized to produce high efficiency devices: no $TiCl_4$ treatment was applied to the TiO_2 film and no scattering layer was used to improve light collection. The *IV* plots of the best four performing cells and the average photovoltaic performance characteristics of these devices were reported in Figure 6.

The two types of cells were found to be characterized with similar open circuit voltage (V_{oc}) and fill factor (FF). However, quite unexpectedly, the P25-based photoanodes, known to contain a significant fraction of rutile TiO_2 of lower bandgap (compared to the anatase phase), showed slightly higher photovoltage for each immersion time. This small difference may be attributed to lower series resistance through the P25-based photoanodes. The short circuit current density (J_{sc}) and the efficiency of cells increased with the immersion time for both types of cells in correlation with an increase in dye loading. Also mirroring the results obtained with the dye desorption study, cells built on PEG 30 photoanodes were found to have significantly higher J_{sc} at 30 mins and 1 hr immersion compared to cells built with DSL 18 NR-AO photoanodes. This difference is related to the faster diffusion and initial anchoring of dye molecules through P25-based films. Finally, at 24 hrs immersion, the DSL 18 NR-AO cells were found to have a slightly higher J_{sc} compared to the P25-based cell. This may be related to (1) the larger surface area and hence dye loading of DSL 18 NR-AO photoanodes (52.9 m^2/g) compared to PEG 30 photoanodes (44.8 m^2/g) and (2) the slightly larger thickness of DSL 18 NR-AO photoanodes which may also contribute, to a lesser extent, to a better average cell performance. Although the actual performance of the cells reported here (which is thought to have been affected by impurities present in the electrolyte) is lower than record literature efficiencies, this study shows a strong correlation between the diffusion and first anchoring phase of dye molecules in DSC photoanodes and the pore characteristics of the TiO_2 films. Also, it should be considered that the architecture of the TiO_2 photoanodes may be modified to better suit large scale manufacturing of liquid DSC devices.

4. Conclusion

Titania films produced from low-cost P25-based aqueous pastes and the commercial DSL 18 NR-AO product were characterized in terms of thickness, porosity, pore size distribution, and surface area. The same films were submitted to dye

uptake measurements and evaluated as photoanodes used for the fabrication of dye-sensitized solar cells. P25-based films were characterized with higher porosity (59.8 to 63.2% versus 56.6%) and a larger fraction of macropores (0.67 to 0.73 versus 0.23) but a slightly lower surface area (42.6 to 44.8 m^2/g versus 52.9 m^2/g) when compared to DSL 18 NR-AO films. These properties, in particular the macroporous component of the films, were found to be critical to the kinetics of dye diffusion during the dye sensitization process. A level of dye saturation through the film >90% was achieved more than 7 times faster in the case of a PEG 30 film compared to a DSL 18 NR-AO film. This result is of great interest for the upscaling of the fabrication of DSC photoanodes. For roll-to-roll manufacturing, it is desirable that this process occurs in seconds and it seems likely that the high porosity films combined with other recent discoveries on fast dyeing could allow this final bottleneck to be overcome. In terms of DSC performance, at short dye immersion times, cells built with PEG 30 photoanodes showed much higher photocurrent (over double) than cells built with DSL 18 NR-AO photoanodes. At standard immersion time of 24 hrs, cells built with DSL 18 NR-AO photoanodes were found to offer slightly higher J_{sc} but almost comparable efficiency compared to cells built with PEG 30 photoanodes. This is almost exclusively related to the difference in surface area available for dyeing and thickness of the titania films, compensated by the higher V_{oc} P25-based films. Further work is in progress to establish how these water-based pastes perform in multiple layers and when submitted to an alternative fast NIR sintering method. Recent work also demonstrated that the P25 product may be combined with smaller TiO_2 (3–5) nanoparticles to form a scaffold with a much higher surface area (up to 85 m^2/g) compared to P25 alone, while maintaining a porous structure characterized with a large fraction of macropores [27]. These scaffolds not only can be sintered by NIR in 12 s only but also may allow much higher levels of dye loading and improved power conversion efficiencies. In addition, recent exciting developments on the use of solid electrolytes or cobased liquid electrolytes in highly porous TiO_2 photoanodes [4, 28] indicate that the P25-based macroporous films presented here could be an attractive development for low-cost scale-up of high efficiency dye-sensitized solar cells. In addition, the relative simplicity of the water-based PEG 30 paste is attractive from a commercial perspective as it is very simple to manufacture; it is also highly relevant for the fabrication of the more recent lead-halide perovskite photovoltaic technologies.

Competing Interests

The authors declare that they have no competing interests.

References

[1] H. J. Snaith, "Perovskites: the emergence of a new era for low-cost, high-efficiency solar cells," *Journal of Physical Chemistry Letters*, vol. 4, no. 21, pp. 3623–3630, 2013.

[2] http://www.nrel.gov/ncpv/images/efficiency_chart.jpg.

[3] B. O'Regan and M. Grätzel, "A low-cost, high-efficiency solar cell based on dye-sensitized colloidal TiO_2 films," *Nature*, vol. 353, no. 6346, pp. 737–740, 1991.

[4] S. Mathew, A. Yella, P. Gao et al., "Dye-sensitized solar cells with 13% efficiency achieved through the molecular engineering of porphyrin sensitizers," *Nature Chemistry*, vol. 6, no. 3, pp. 242–247, 2014.

[5] D. Joly, L. Pellejà, S. Narbey et al., "A robust organic dye for dye sensitized solar cells based on iodine/iodide electrolytes combining high efficiency and outstanding stability," *Scientific Reports*, vol. 4, article 4033, 2014.

[6] W. Xiang, W. Huang, U. Bach, and L. Spiccia, "Stable high efficiency dye-sensitized solar cells based on a cobalt polymer gel electrolyte," *Chemical Communications*, vol. 49, no. 79, pp. 8997–8999, 2013.

[7] S. Dai, J. Weng, Y. Sui et al., "The design and outdoor application of dye-sensitized solar cells," *Inorganica Chimica Acta*, vol. 361, no. 3, pp. 786–791, 2008.

[8] P. Mariani, L. Vesce, and A. Di Carlo, "The role of printing techniques for large-area dye sensitized solar cells," *Semiconductor Science and Technology*, vol. 30, no. 10, Article ID 104003, 2015.

[9] S. Yoon, S. Tak, J. Kim, Y. Jun, K. Kang, and J. Park, "Application of transparent dye-sensitized solar cells to building integrated photovoltaic systems," *Building and Environment*, vol. 46, no. 10, pp. 1899–1904, 2011.

[10] A. Reale, L. Cinà, A. Malatesta, R. De Marco, T. M. Brown, and A. Di Carlo, "Estimation of energy production of dye-sensitized solar cell modules for building-integrated photovoltaic applications," *Energy Technology*, vol. 2, no. 6, pp. 531–541, 2014.

[11] T. Watson, I. Mabbett, H. Wang, L. Peter, and D. Worsley, "Ultrafast near infrared sintering of TiO_2 layers on metal substrates for dye-sensitized solar cells," *Progress in Photovoltaics: Research and Applications*, vol. 19, no. 4, pp. 482–486, 2011.

[12] M. Cherrington, T. C. Claypole, D. Deganello, I. Mabbett, T. Watson, and D. Worsley, "Ultrafast near-infrared sintering of a slot-die coated nano-silver conducting ink," *Journal of Materials Chemistry*, vol. 21, no. 21, pp. 7562–7564, 2011.

[13] P. J. Holliman, M. L. Davies, A. Connell, B. V. Velasco, and T. M. Watson, "Ultra-fast dye sensitisation and co-sensitisation for dye sensitized solar cells," *Chemical Communications*, vol. 46, no. 38, pp. 7256–7258, 2010.

[14] P. J. Holliman, M. Mohsen, A. Connell et al., "Ultra-fast co-sensitization and tri-sensitization of dye-sensitized solar cells with N719, SQ1 and triarylamine dyes," *Journal of Materials Chemistry*, vol. 22, no. 26, pp. 13318–13327, 2012.

[15] P. J. Holliman, K. J. Al-Salihi, A. Connell, M. L. Davies, E. W. Jones, and D. A. Worsley, "Development of selective, ultra-fast multiple co-sensitization to control dye loading in dye-sensitized solar cells," *RSC Advances*, vol. 4, no. 5, pp. 2515–2522, 2014.

[16] M. L. Davies, T. M. Watson, P. J. Holliman, A. Connell, and D. A. Worsley, "In situ monitoring and optimization of room temperature ultra-fast sensitization for dye-sensitized solar cells," *Chemical Communications*, vol. 50, no. 83, pp. 12512–12514, 2014.

[17] M. Dürr, A. Schmid, M. Obermaier, A. Yasuda, and G. Nelles, "Diffusion properties of dye molecules in nanoporous TiO_2 networks," *Journal of Physical Chemistry A*, vol. 109, no. 17, pp. 3967–3970, 2005.

[18] J. J. Nelson, T. J. Amick, and C. M. Elliott, "Mass transport of polypyridyl cobalt complexes in dye-sensitized solar cells

with mesoporous TiO_2 photoanodes," *The Journal of Physical Chemistry C*, vol. 112, no. 46, pp. 18255–18263, 2008.

[19] D. M. Xie, S. Feng, Y. Lin et al., "Preparation of porous nanocrystalline TiO_2 electrode by screen-printing technique," *Chinese Science Bulletin*, vol. 52, no. 18, pp. 2481–2485, 2007.

[20] K.-M. Lee, V. Suryanarayanan, and K.-C. Ho, "The influence of surface morphology of TiO_2 coating on the performance of dye-sensitized solar cells," *Solar Energy Materials and Solar Cells*, vol. 90, no. 15, pp. 2398–2404, 2006.

[21] D. Zhang, S. Ito, Y. Wada, T. Kitamura, and S. Yanagida, "Nanocrystalline TiO_2 electrodes prepared by water-medium screen printing technique," *Chemistry Letters*, no. 10, pp. 1042–1043, 2001.

[22] T. Ma, T. Kida, M. Akiyama et al., "Preparation and properties of nanostructured TiO_2 electrode by a polymer organic-medium screen-printing technique," *Electrochemistry Communications*, vol. 5, no. 4, pp. 369–372, 2003.

[23] D. S. Tsoukleris, I. M. Arabatzis, E. Chatzivasiloglou et al., "2-Ethyl-1-hexanol based screen-printed titania thin films for dye-sensitized solar cells," *Solar Energy*, vol. 79, no. 4, pp. 422–430, 2005.

[24] T. Watson, P. Holliman, and D. Worsley, "Rapid, continuous in situ monitoring of dye sensitisation in dye-sensitized solar cells," *Journal of Materials Chemistry*, vol. 21, no. 12, pp. 4321–4325, 2011.

[25] C. S. Kong, D.-Y. Kim, H.-K. Lee, Y.-G. Shul, and T.-H. Lee, "Influence of pore-size distribution of diffusion layer on mass-transport problems of proton exchange membrane fuel cells," *Journal of Power Sources*, vol. 108, no. 1-2, pp. 185–191, 2002.

[26] W.-W. Xue, L.-H. Hu, S.-Y. Dai, C.-N. Zhang, X. D. Luo, and W.-P. Jing, "A study on porosity distribution in nanoporous TiO_2 photoelectrodes for output performance of dye-sensitized solar cells," *Chinese Physics Letters*, vol. 27, no. 3, Article ID 038202, 2010.

[27] C. Charbonneau, P. J. Holliman, M. L. Davies, T. M. Watson, and D. A. Worsley, "Facile self-assembly and stabilization of metal oxide nanoparticles," *Journal of Colloid and Interface Science*, vol. 442, pp. 110–119, 2015.

[28] I. Chung, B. Lee, J. He, R. P. H. Chang, and M. G. Kanatzidis, "All-solid-state dye-sensitized solar cells with high efficiency," *Nature*, vol. 485, no. 7399, pp. 486–489, 2012.